Chen *et al. Int J Concr Struct Mater* (2022) 16:61
https://doi.org/10.1186/s40069-022-00547-3

International Journal of Concrete Structures and Materials

RESEARCH Open Access

Experimental and Numerical Investigation of the Tensile Performance and Failure Process of a Modified Portland Cement

Jianhang Chen[1,2], Kangming Tao[2], Banquan Zeng[2], Lei Liu[2], Hongbao Zhao[1,2], Junwen Zhang[1,2*] and Danqi Li[3*]

Abstract

A better understanding of the tensile performance and tensile failure mechanism of cement paste is significant in preventing rock reinforcement failure. Therefore, this paper aims to reveal the tensile performance and failure mechanism of a modified Portland cement: Stratabinder HS cement. To achieve this objective, the split tensile test was conducted on specimens followed by simulating the failure mechanism numerically. The results indicated that the water–cement rate significantly influenced the tensile performance of the cement paste. When the water–cement rate increased from 0.35 to 0.42, the tensile strength declined from 1.9 MPa to 1.5 MPa. It was also observed that vertical tensile failure constantly occurred regardless of the water–cement rate. During the testing process, tensile cracks and shear cracks occurred. The increasing rate in the number of specimen cracks was dependent on the tensile stress state. Before the tensile stress reached the peak, the crack quantity increased slightly. After the peak, the crack quantity increased dramatically. During the vertical loading process, horizontal tensile stress occurred in the specimen. This horizontal tensile stress zone showed a diamond shape. The higher the tensile stress is, the larger the area of the horizontal tensile stress zone. When the tensile strength was reached, horizontal tensile stress mainly concentrated at the vertical centre of the specimen. This finally led to tensile failure of the specimen. This paper indicated that the water–cement rate was the key factor in evaluating the tensile strength of the Stratabinder HS cement.

Keywords: Cement paste, Tensile strength, Tensile failure, Fractures, Water–cement rate

1 Introduction

Portland cement is an indispensable binding material in engineering projects. In civil engineering, Portland cement is used to fabricate concretes (Jung et al., 2018; Murmu & Singh, 2014). In mining engineering, Portland cement plays a paramount role in guaranteeing underground excavation safety (Chen & Li, 2022; Chen et al., 2020; Wu et al., 2019). For example, Portland cement can be used to fill discontinuities in jointed rock masses around excavations to improve rock stability (Aili & Maruyama, 2020; Aziz et al., 2017).

A better understanding of the mechanical properties of Portland cement is beneficial for promoting its value in use. It is noteworthy that the majority of the attention was given to Portland cement's uniaxial compressive strength (UCS) (Rashad et al., 2014). Only limited work has been performed to analyse its tensile strength.

In fact, Portland cement's tensile performance is crucial in engineering applications. In rock reinforcement, Portland cement fills the annulus between the rock tendon and rock mass (Li et al., 2021). After the rock tendon is loaded, radial dilation occurs at the tendon-to-grout interface (Fig. 1). This dilation leads to tensile

Journal information: ISSN 1976-0485/eISSN 2234-1315

*Correspondence: zhangjw@cumtb.edu.cn; danqi.li@curtin.edu.au

[1] State Key Laboratory for Geomechanics and Deep Underground Engineering, China University of Mining and Technology (Beijing), Beijing 100083, China
[3] Energy and Chemical Engineering, WA School of Mines: Minerals, Curtin University, Kalgoorlie, WA 6430, Australia
Full list of author information is available at the end of the article

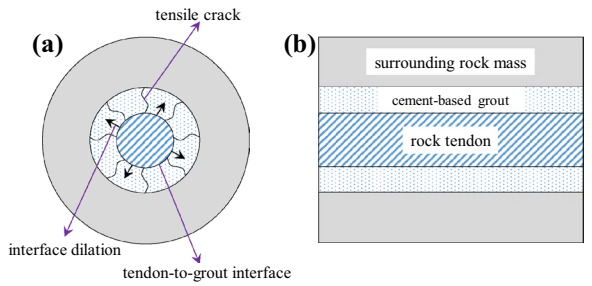

Fig. 1 Rock reinforcement system **a** cross-sectional view; **b** lateral view.

cracks in the cement-based grout (Chen et al., 2021). These tensile cracks may jeopardise the capacity of the rock reinforcement system (Chen et al., 2022; Skrzypkowski, 2021; Wu et al., 2018).

To evaluate the tensile performance of the cement, experimental tests were more widely used. Two different test methods can be used: the split tensile strength (STS) test or the direct uniaxial tensile strength (UTS) test (Bybee, 2004). With these two methods, researchers compared the tensile performance of different cements (Paknahad et al., 2020). Bayindir et al. (2009) indicated that the cement type significantly influenced the tensile strength of the cement paste. Bybee (2004) found that fibre-reinforced cement had higher tensile strength than plain cement. In contrast, Syarif et al. (2018) indicated that the organic cement had a smaller strength than the normal Portland cement.

Attention was also given to the influence of additives on the tensile performance of cement pastes. Mishra and Kantharia (2021) indicated that adding nanozinc oxide increased the tensile strength of the cement. Similarly, adding carbon nanotubes increased the tensile strength of the cement as well (Silvestro & Gleize, 2020).

Additional attention was given to the influence of cement proportion (Fedrigo et al., 2018), porosity (Chen et al., 2013), curing time (Wang et al., 2020), temperature (Masoud et al., 2010), saturation condition (Gu et al., 2019), loading condition (Liu et al., 2019), specimen size (Xiong & Geng, 2020) and the use of aggregates (Bitouri et al., 2017) on the tensile performance of cement. The results showed that the tensile strength of the cement paste was critically influenced by various parameters. Therefore, to optimise the tensile strength of the cement paste, the corresponding test condition and environment should be strictly controlled.

In recent years, researchers have also studied the tensile performance of cement at the microscale. Němeček et al. (2016) indicated that the tensile performance of the cement at the microscale was largely different from that at the macroscale.

The above research provided valuable knowledge in revealing the tensile performance of cement. Recently, a modified Portland cement named the Stratabinder HS cement has been widely applied in civil and mining projects. However, little work has been reported on its tensile performance. Moreover, little research has been conducted to use the discrete element method (DEM) to evaluate the tensile failure of cement. Considering that failure of the material plays a significant role in engineering applications (Song & Zhang, 2022), this paper adopted experimental and numerical methods to analyse the tensile performance of Stratabinder HS cement.

The experimental program was first illustrated. Then, the experimental results and data analysis were presented, followed by numerical simulation results. Finally, further studies were recommended.

2 Experimental Program

2.1 Materials

This study aims to evaluate the tensile performance of the Stratabinder HS cement. To fulfil this purpose, fresh Stratabinder HS cement was ordered from the Minova Company.

The Stratabinder HS cement is generally composed of two parts. One is Portland cement, accounting for more than 60%. The other is the nonhazardous ingredients, accounting for the remaining proportion. The chemical composition of the Stratabinder HS cement mainly includes calcium oxide, silica, alumina and iron oxide.

In situ observation shows that when this cement is used, a key factor is the water–cement rate. In this study, two different water–cement rates were used. One was 0.35, and the other was 0.42. The reason to use those two water–cement rates is that if the cement paste is too thick (water–cement rate < 0.3), cement mixing is a problem without the water reducing agent added. Previous research indicated that once the water reducing agent was added, a solvation thin film was generated around the cement particles. This solvation thin film reduced the friction resistance of the cement particles. Therefore, with the water reducing agent added, the cement paste could be properly mixed even when the water–cement rate was smaller than 0.3 (Şahin et al., 2022).

In contrast, if the cement paste is too thin (water–cement rate > 0.5), the strength of the cement paste may not meet the engineering quality requirement.

2.2 Experimental UCS Test

First, the UCS test was conducted to evaluate the compressive performance of the Stratabinder HS cement.

During the experimental UCS test, cylinder specimens with a diameter of 54 mm and height of 142 mm were cast with cylindrical moulds. Two water–cement rates of 0.35 and 0.42 were used. After all specimens were fully cured for 28 days, a griding machine was used to polish two ending surfaces of the specimen. Then, those cylinder specimens were placed in the MTS 815 machine to conduct UCS tests, as shown in Fig. 2.

The UCS test was used to calibrate and confirm the later numerical simulation. Specific information of the experimental UCS test can be found in Chen et al. (2014).

2.3 Experimental Tensile Test

2.3.1 Selection of the Tensile Test Method

Although either the UTS or STS test method can be used to measure the tensile strength of cement, the UTS method is more difficult to conduct (Sun & Wu, 2021). This is because during the UTS test, specimens should be clamped by the gripping device, leading to the stress concentration occurrence at the specimen's corner. Therefore, it is possible that the specimen may fail due to stress concentration rather than tensile stress.

Fig. 2 Experimental UCS test.

In contrast, the STS test method is relatively easier. Therefore, in this paper, the STS test method was adopted.

2.3.2 Test Specimen Preparation

PVC tubes were used as the casting mould. They had a height of 110 mm and internal diameter of 42 mm. This casting mould was adhered to a wooden board to prevent cement leakage. Moreover, the internal surface of this casting mould was brushed with a thin oil. This is to avoid the cement paste sticking onto the casting mould after demoulding.

After the Stratabinder HS cement was mixed with water, the cement paste was poured into the casting mould. Then, the casting mould was placed on a vibrator. The vibrator was switched on, and the casting mould was vibrated for 1 min. The purpose is to remove air voids in the cement paste.

After setting for 24 h, the specimen was demoulded. All specimens were immersed in fresh water for curing. After 28 days, they were removed from the water. Then, specimens were fixed on a lathe. An electric saw was used to cut the specimens into disks. Finally, all disk specimens had a diameter of approximately 42 mm and a thickness of approximately 25 mm. The height/diameter rate was approximately 0.59.

To confirm that the results are reliable, at least 5 specimens were prepared for each water–cement rate. The prepared specimens at a w/c rate of 0.35 are shown in Fig. 3.

2.3.3 Experimental Test Process

Each specimen was installed in an MTS 815 testing machine, as shown in Fig. 4.

This machine was equipped with the servo controlling system. A displacement control can be applied in the full testing process. When conducting this STS test, a constant velocity of 3 μm/s was applied to the specimen. A load cell was set on the bottom plate to record the vertical force. In addition, the displacement transducer in

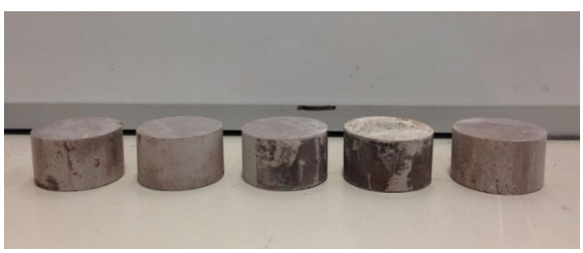

Fig. 3 Prepared specimens.

Fig. 4 Split tensile strength test.

the testing machine automatically recorded the vertical displacement.

Equation (1) was used to calculate the tensile stress in the specimen:

$$\sigma_t = \frac{2F}{\pi Dt} \tag{1}$$

where σ_t is the tensile strength of the specimen; F is the vertical force that was applied on the specimen; D is the specimen diameter; and t is the specimen thickness.

Since the data logger system automatically recorded the force–displacement curve, the tensile stress–displacement result can be calculated with Eq. (1).

3 Experimental Results

3.1 UCS Test Results

The experimental UCS tests showed that the specimen had a UCS of 63.1 MPa at a water–cement rate of 0.35. In contrast, the specimen showed a UCS of 54.3 MPa at a water–cement rate of 0.42 (Table 1).

Table 1 Experimental UCS test results.

Water–cement rate	UCS (MPa)	*E* (GPa)	*μ*
0.35	63.1	11.8	0.23
0.42	54.3	9.9	0.21

where *E* is the Young's modulus, *μ* is the Poisson's ratio

3.2 Tensile Test Results

3.2.1 Tensile Stress–Displacement Results

After the STS test, the results for the cement paste with a water–cement rate of 0.35 are summarised in Table 2.where SD is the standard deviation and SEM is the standard error of the mean. These two parameters were calculated with Eqs. (2) and (3):

$$SD = \sqrt{\frac{\sum \left(\sigma_{ti} - \bar{\sigma_t}\right)^2}{n}} \tag{2}$$

$$SEM = \frac{S}{\sqrt{n}} \tag{3}$$

where σ_{ti} is the peak tensile stress of specimens; $\bar{\sigma_t}$ is the average tensile strength of specimens; and n is the number of repetition tests.

The tensile strength of the specimens ranged between 1.3 MPa and 4.2 MPa. The SD was 1.03, and the SEM was 0.46. Considering that random results may occur, the data were further processed to guarantee the consistency of the testing results. The maximum value and minimum value were removed. The peak tensile stress of the remaining three specimens was averaged with Eq. (4) as the tensile strength:

$$\sigma_{tave} = \frac{\sigma_{t1} + \sigma_{t2} + \sigma_{t3}}{3} \tag{4}$$

where σ_{tave} is the average tensile strength of the remaining specimens.

Consequently, the average tensile strength was 1.9 MPa. The tensile stress–displacement curves are shown in Fig. 5.

This shows that with increasing displacement, the tensile stress of the specimen increased nonlinearly before its peak. After the tensile stress reached its peak, the tensile stress of the specimen declined dramatically. The specimen may reach the initial peak when the displacement reaches approximately 0.2 mm, followed by a sharp decline in the bearing capacity. The specimen's carrying capacity rose again until reaching its global peak value at approximately 0.4 mm.

During testing, the deformation of the MTS 815 machine itself was ignored, as the loading frame is much stiffer than the test specimen.

It is also noteworthy that additional methods were employed to minimise the gap between the test specimen and loading frame before the test. The test specimen

Table 2 STS test results when the water–cement rate was 0.35.

No.	*t* (mm)	*D* (mm)	*t*/*D* rate	σ_t (MPa)	SD	SEM
1	24.4	42.3	0.58	1.6	1.03	0.46
2	25.6	41.0	0.63	2.1		
3	24.8	41.3	0.6	4.2		
4	24.3	41.5	0.59	1.9		
5	24.3	41.7	0.58	1.3		

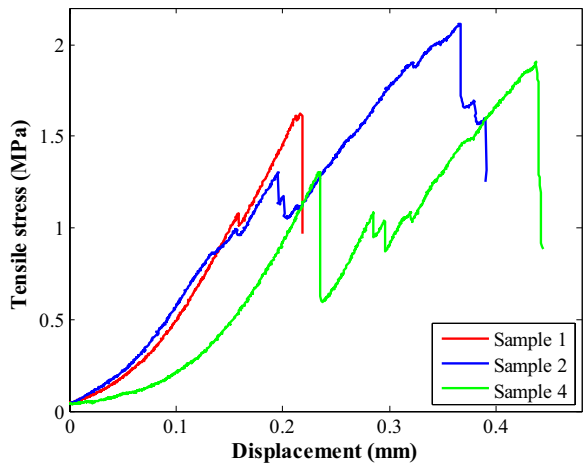

Fig. 5 Tensile stress–displacement curves when the water–cement rate was 0.35.

Fig. 6 Failure state in the STS test.

was placed underneath the loading plate in the machine. The bottom plate was lifted until the smallest visible gap formed. Then, the bottom plate was further lifted with the help of the micro-displacement control in the computer interface so that a very small positive load was applied to the specimen. By doing this, tight but not excessive contact between the specimen and loading frame could be formed. This would guarantee the accuracy of the testing results by ensuring that any displacement in the specimen would lead to a change in the stress.

After the STS test, a typical failure mode is shown in Fig. 6. Apparently, vertical failure was generated at the specimen centre. The two sides of the specimen tended to separate along the horizontal direction.

Further tests were conducted on specimens with a water–cement rate of 0.42. The results are summarised in Table 3.

For the water–cement rate of 0.42, the specimen's tensile strength ranged between 0.7 MPa and 1.9 MPa. The SD was 0.43, and the SEM was 0.19. To remove random results, the minimum values and maximum values were eliminated. Then, the tensile strength of the cement paste with a water–cement rate of 0.42 was 1.5 MPa. The tensile stress–displacement curves of the remaining specimens are plotted in Fig. 7.

Apparently, for the water–cement rate of 0.42, the tensile stress–displacement curves were smoother. With increasing displacement, the tensile stress of the specimen continuously increased. After the specimen reached the tensile strength, the carrying capacity of the specimens declined dramatically.

3.2.2 The Impact of the Water–Cement Rate

Previous research has been conducted to evaluate the impact of the water–cement rate on the tensile performance of normal Portland cement. It showed that there was an adverse impact of the water–cement rate on the tensile strength (Hyett et al., 1992).

Following similar procedures, the impact of the water–cement rate on the tensile performance of the Stratabinder HS cement was analysed. As shown in Fig. 8, there was a strong relationship between the water–cement rate and the tensile strength of the Stratabinder HS cement. As the water–cement rate increased, the tensile strength of the cement decreased. This result agreed well with the in situ observation results. Specifically, for a high water–cement rate used in rock reinforcement, tensile failure of the cement grout annulus was more likely to occur.

Table 3 STS test results when the water–cement rate was 0.42.

No.	*t* (mm)	*D* (mm)	*t*/*D* rate	σ_t (MPa)	SD	SEM
1	25.0	42.1	0.59	1.8	0.43	0.19
2	25.4	41.8	0.61	0.7		
3	24.8	42.2	0.59	1.9		
4	24.9	41.9	0.59	1.3		
5	25.1	42.1	0.6	1.4		

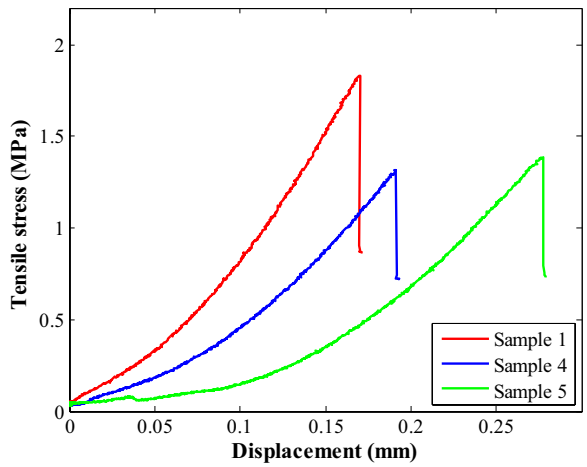

Fig. 7 Tensile stress–displacement curves when the water–cement rate was 0.42.

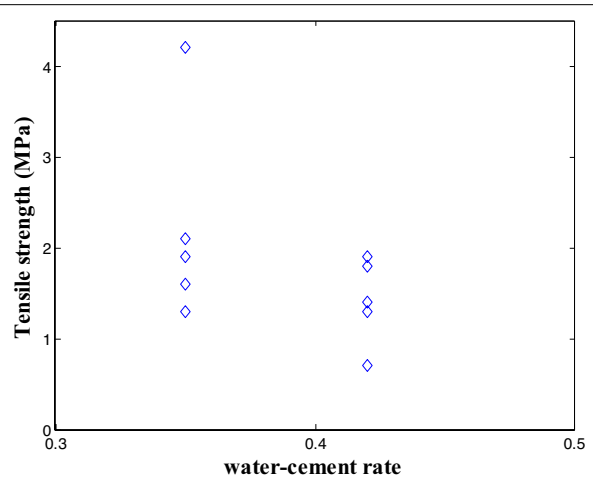

Fig. 8 Impact of the water–cement rate on the tensile strength of the Stratabinder HS cement.

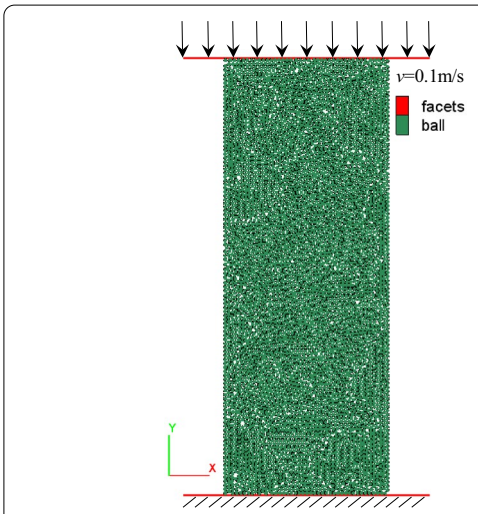

Fig. 9 Numerical simulation of the UCS test.

3.3 Numerical Simulation Scheme

Numerical simulation was conducted, because it is powerful in revealing the microscopic failure behaviour of materials (Chen et al., 2019; Wang et al., 2021). In addition, numerical simulation was able to reproduce the tensile failure process of the cement paste.

3.4 Selection of the Numerical Code

Among all numerical simulation methods, the DEM was adopted. The reason is that the DEM assumes that the numerical zones are discrete. Moreover, the bond between numerical zones is allowed to break when subjected to loading. As such, it is believed that tensile failure of the cement paste can be more closely simulated with DEM. For the software, the Particle Flow Code (PFC) was used.

3.5 Simulation Process

Initially, the cement paste with a water–cement rate of 0.35 was simulated. In PFC, properties of the particles, including the effective modulus and stiffness rate, should be input. These properties can be acquired by conducting numerical UCS tests.

First, a rectangular domain with an edge length of 100 mm was created. Then, the numerical UCS specimen was created in this domain, as shown in Fig. 9. This numerical specimen had a height of 142 mm and

a width of 54 mm. Moreover, its dimension was consistent with the size used in laboratory tests. This numerical specimen was composed of 5188 balls. The ball radius ranged between 0.6 mm and 0.7 mm. The porosity of this numerical specimen was 0.1. After this numerical specimen was created, this model was solved automatically until the averaged unbalanced force ratio decreased to 1×10^{-5} to eliminate the overlap between balls.

The bottom boundary of the specimen was fixed to support the numerical specimen. Meanwhile, a constant compressive velocity of 0.1 m/s was applied on the top boundary of the specimen. During the test, the applied force and vertical deformation were recorded. In addition, the increment of the specimen's width at the middle section was recorded.

Based on the recorded information, the axial stress of the specimen can be calculated with Eq. (5):

$$\sigma_c = \frac{F}{Wt} \tag{5}$$

where σ_c is the compressive stress of the specimen; W is the specimen width; t is the specimen thickness, equalling 1 in this two-dimensional simulation.

The compressive strain or the axial strain of the specimen can be calculated with Eq. (6):

$$\varepsilon_a = \frac{\Delta H}{H} \tag{6}$$

where ε_a is the compressive strain or axial strain; ΔH is the variation of the specimen height; and H is the specimen height.

The tensile strain or diametric strain of the specimen can be calculated with Eq. (7):

$$\varepsilon_d = \frac{\Delta W}{W} \tag{7}$$

where ε_d is the diametric strain; ΔW is the variation of the specimen width.

Then, Poisson's ratio of the specimen can be calculated with Eq. (8):

$$\mu = -\frac{\varepsilon_d}{\varepsilon_a} \tag{8}$$

where μ is the Poisson's ratio.

The flat joint model was used to simulate the particles' contact behaviour. Then, the input parameters were calibrated until the numerical results fit well with the experimental results.

By conducting numerical UCS tests, input parameters, including the stiffness rate, surface gap, friction coefficient, cohesion and friction angle, can be determined.

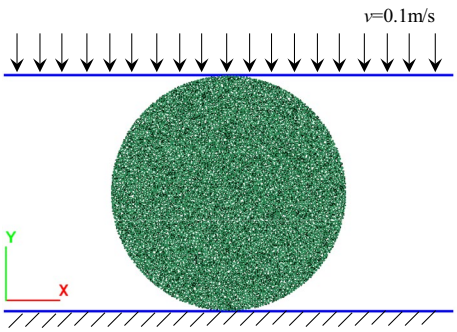

Fig. 10 Numerical STS test created in PFC.

Then, the numerical STS test was performed. Specifically, a disk geometry was created (Fig. 10). In this simulation, the specimen diameter was 42 mm. This was the same as the geometric size in the experimental STS test.

The bottom boundary in the numerical STS test was fixed. Then, a constant compressive velocity of 0.1 m/s was applied on the top boundary. During loading, the vertical force and displacement were monitored. Then, Eq. (1) was used to calculate the tensile stress.

The input parameters, including the stiffness rate, surface gap, friction coefficient, cohesion and friction angle, were directly acquired from the numerical UCS test. The input parameter of tensile strength was calibrated until the numerical tensile stress–displacement curve fit well with the experimental curve.

4 Numerical Simulation Results and Analysis

Following the above simulation procedures, input factors for two different water–cement rates were obtained, as summarised in Table 4. For the numerical test, there was an apparent difference in the mechanical properties of the specimen.

Among the above parameters, the stiffness rate represents the relative rate between the normal stiffness and shear stiffness. The surface gap represents the maximum gap interval to bond the numerical balls. The friction coefficient represents the factor that is used to calculate the friction resistance between numerical balls in the postfailure stage. The cohesion represents the cohesive strength between numerical balls before shear bond breaks. The friction angle represents the factor that is used to calculate the friction resistance between numerical balls before shear bond breaks.

Table 4 Input factors for the cement paste.

Water–cement rate	Effective modulus (GPa)	Stiffness rate	Surface gap	Friction coefficient	Cohesion (MPa)	Friction angle (°)
0.35	6.5	1.18	1×10^{-4}	0.3	26	10
0.42	4.8	1.13	1×10^{-4}	0.3	18	8

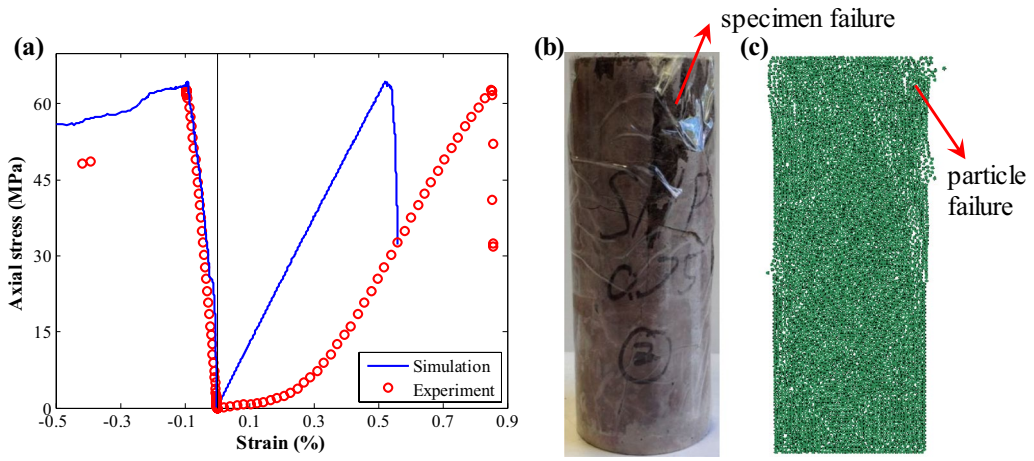

Fig. 11 Comparison between the numerical and experimental UCS results when the water–cement rate was 0.35: **a** stress–strain curves; **b** experimental failure mode; **c** numerical failure mode.

Then, the axial stress–strain curves of the specimen can be acquired. When the water–cement rate was 0.35, the axial stress–strain curve of the cement paste is plotted in Fig. 11a.

The numerical simulation showed that the UCS, Young's modulus and Poisson's ratio were 64.5 MPa, 12.3 GPa and 0.22, respectively. The relative differences between the numerical simulation and experimental test were 2.2%, 4.2% and 4.3%. There was a close match between them. This validated that the input parameters were effective in analysing the compressive performance of the cement paste.

Moreover, the UCS failure mode comparison when the water–cement rate was 0.35 is shown in Fig. 11b, c. In the experiment, part of the cement paste was ejected from the specimen. This phenomenon also occurred in the numerical simulation. Apparently, in the numerical simulation, some of the particles detached from the numerical specimen. Therefore, there was a general consistency between the experimental and numerical failure modes.

Then, those input parameters were substituted into the numerical STS test. Calibration was conducted on the input parameter of the tensile strength. When the input parameter of tensile strength equalled 2.38 MPa, a satisfactory match between the numerical and experimental results was acquired (Fig. 12).

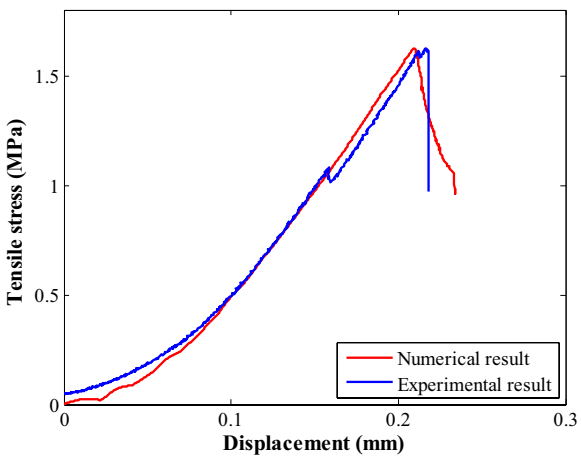

Fig. 12 Tensile stress–displacement curve comparison when the water–cement rate was 0.35.

At the end of this numerical STS test, the specimen failure mode was checked (Fig. 13).

There was an apparent vertical tensile failure at the middle of this specimen. Comparing it with the experimental failure mode, there was a close match between them. This further confirmed the accuracy of this numerical STS test.

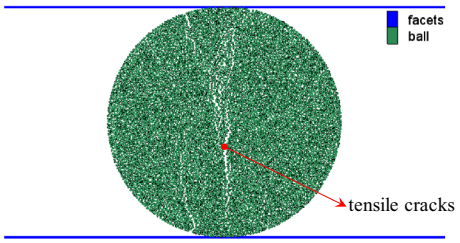

Fig. 13 Failure state when the water–cement rate was 0.35.

An advantage of the numerical simulation is that it can reveal the microscopic failure behaviour of the material. Since the created numerical model has been successfully validated with experimental tests, it was further used to reveal the microscopic failure of the cement paste. The fractures in the specimen were recorded. At the end of this numerical STS test, those fractures are plotted in Fig. 14. Apparently, along the vertical direction, a number of cracks were generated in the central part of the specimen. Tensile cracks occurred at the top, middle and bottom sections of the specimen. More interestingly, there were also several shear cracks. This indicated that during the STS test, shear failure of the particles may also occur.

The variation in the fracture quantity was also checked (Fig. 15). At the initial loading stage, the number of fractures in the specimen increased slightly. When the time step increased to 53,410, the tensile stress of the specimen reached the tensile strength. Meanwhile, the quantity of fractures arrived at 624, which was still a small value. After that, the quantity of fractures in the specimen increased dramatically. This indicated that the significant increase in the fracture quantity started after the specimen reached the tensile strength.

The other advantage of numerical modelling is that the stress state in the specimen can be exported dynamically. For example, in this case, the horizontal stress state in the specimen when the tensile stress reached 50%, 80% and 100% tensile strength was exported (Fig. 16).

In this figure, positive values represent tensile stress. Although vertical force was applied on the specimen, apparent horizontal tensile stress was generated, as

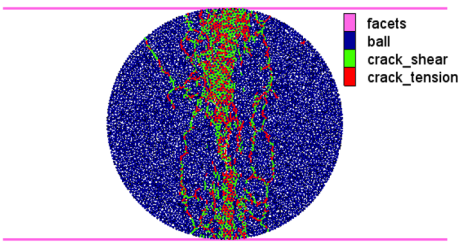

Fig. 14 Crack state when the water–cement rate was 0.5.

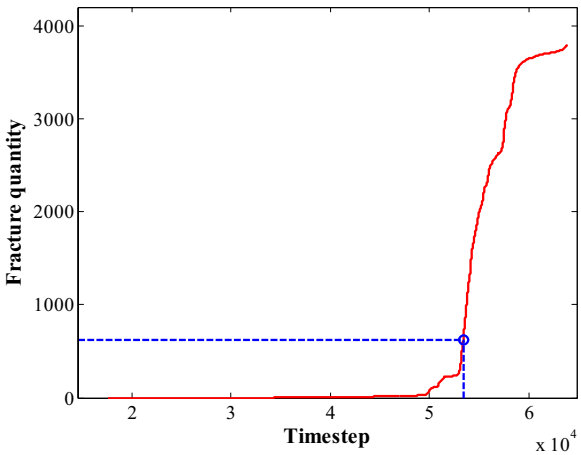

Fig. 15 Increasing process of the fracture quantity in the specimen.

shown in Fig. 16a. Before the tensile stress reached the peak, the horizontal tensile stress showed a diamond shape. With increasing tensile stress, the area of this diamond shape increased, as shown in Fig. 16b. When the tensile stress reached the peak, the diamond shape of the horizontal tensile stress disappeared. Moreover, horizontal tensile stress mainly appeared at the central section of the specimen, as shown in Fig. 16c. With further loading, apparent tensile failure was generated at the middle section of the specimen. The majority of the specimen lost the ability to bear the tensile stress, as shown in Fig. 16d.

Further simulation work was continued to evaluate the tensile performance of the cement paste when the water–cement rate was 0.42. Table 4 summarises the calibrated input parameters.

Then, the specimen's axial stress–strain curve can be acquired. The simulation showed that the UCS, Young's modulus and Poisson's ratio were 54.4 MPa, 10 GPa and 0.22. The relative differences between the numerical and experimental tests were 0.2%, 1.0% and 4.8%. There was a close match between them, as shown in Fig. 17a.

The experimental and numerical UCS failure modes are shown in Fig. 17b, c. In the experiment, part of the cement paste was ejected from the specimen. This was also monitored in the numerical simulation. Specifically, a number of particles detached from the numerical specimen. Therefore, these results were in reasonable agreement.

It is interesting to see that when comparing the experimental and numerical UCS curves, there is an apparent difference in the initial stiffness. Specifically, the initial stiffness obtained from the experiment was much smaller than that obtained from the simulation. The reason is that in the experiment, after the specimens were fully cured, there were still certain air voids in the specimens.

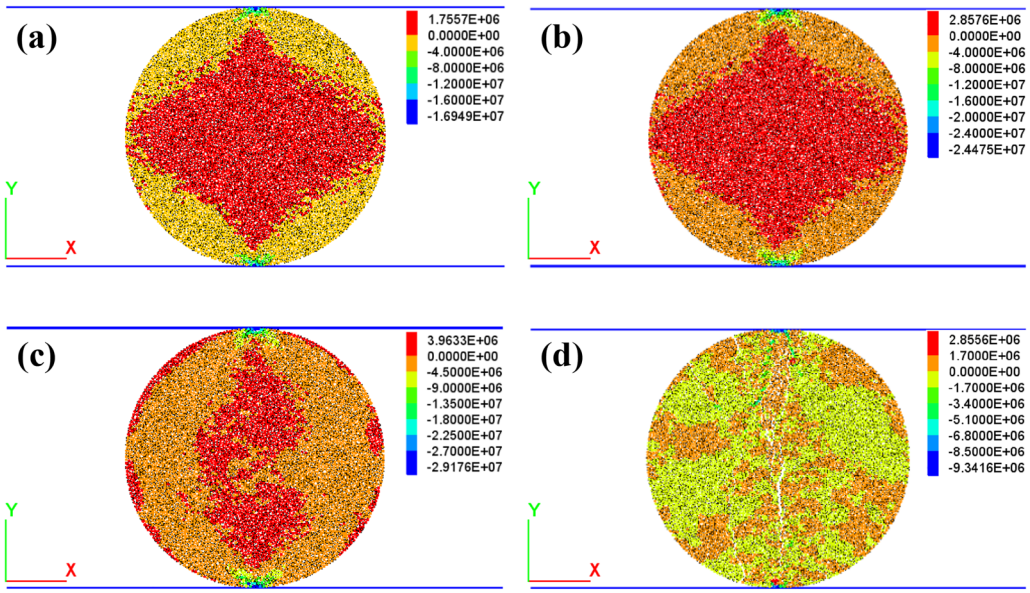

Fig. 16 Horizontal stress state when the water–cement rate was 0.35: **a** 50% tensile strength; **b** 80% tensile strength; **c** 100% tensile strength; **d** after tensile strength.

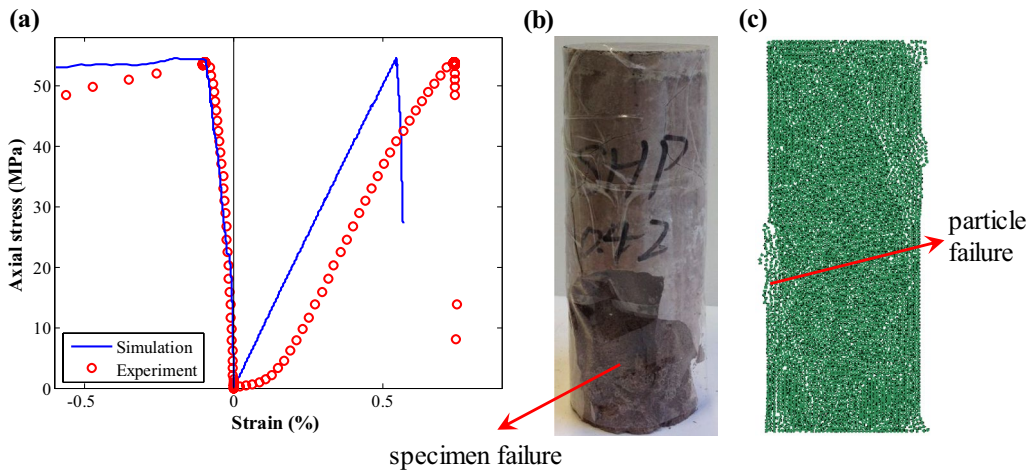

Fig. 17 Comparison between the numerical and experimental UCS results when the water–cement rate was 0.42: **a** stress–strain curves; **b** experimental failure mode; **c** numerical failure mode.

After the experimental UCS test was conducted, these air voids in the specimens were compressed to close. During this period, the bearing capacity of the specimens could only increase gently. Consequently, the initial stiffness of the specimens in the experiment was small. However, after the air voids in the specimens fully closed, the specimens became dense. Then, the bearing capacity of the specimens started increasing dramatically.

In contrast, the numerical specimen is composed of numerous dense particles. Therefore, the air voids in the experimental specimen cannot be simulated with the PFC program. Then, at the initial loading stage of the numerical specimen, the bearing capacity increased dramatically. Consequently, the initial stiffness of the experimental specimen was much smaller than that of the numerical specimen.

Next, a STS test was created in the PFC. The geometry and specimen diameter were consistent with the experimental test. Calibration was conducted on the input parameter of tensile strength. When the input

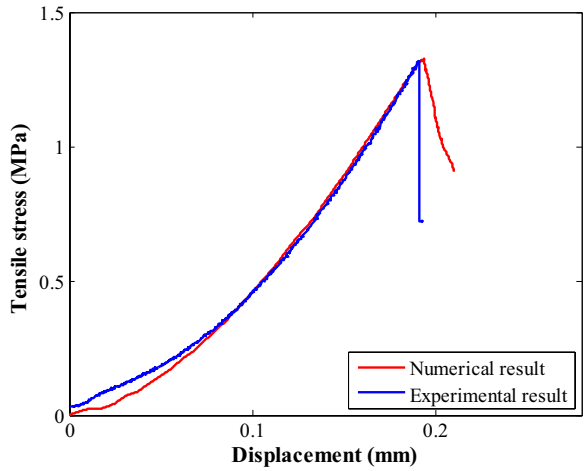

Fig. 18 Numerical and experimental result comparison when the water–cement rate was 0.42.

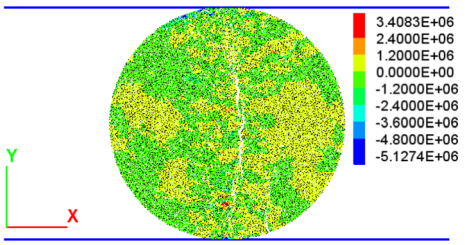

Fig. 20 Horizontal stress state when the water–cement rate was 0.42.

parameter of tensile strength equalled 1.98 MPa, there was a reasonable match between the physical and numerical tests (Fig. 18).

The failure mode and crack state of the specimen were also checked (Fig. 19). After the numerical STS test, apparent tensile failure was generated in the central part of the specimen. Moreover, in the specimen, both tensile and shear cracks occurred.

In the simulation, at the end of the STS test, the horizontal stress state in the specimen was exported (Fig. 20). Since tensile failure was generated in the specimen, the majority of the specimen lost the ability to bear the tensile stress.

5 Discussion

The experimental STS results showed that the tensile performance of the Stratabinder HS cement generally agreed with that of normal Portland cement. For example, Rocha and Ludvig (2017) conducted STS tests on normal Portland cement. They indicated that when the water–cement rate was 0.33, the normal Portland cement showed a tensile strength of 2.13 MPa. For the Stratabinder HS cement, when the water–cement rate was 0.35, the tensile strength was 1.9 MPa.

Moreover, when the water–cement rate changed, the variation trend of the Stratabinder HS cement's tensile strength agreed well with that of normal Portland cement. It is known that as the water–cement rate increases, the tensile strength of normal Portland cement decreases (Hyett et al., 1992). This phenomenon was also monitored when testing the Stratabinder HS cement.

In addition, Hyett et al. (1992) indicated that when normal Portland cement was used, a low water–cement rate was likely to result in a scatter of the tensile strength results. This was also true for the Stratabinder HS cement. When the water–cement rate was 0.42, the standard error of the mean was 0.19. When the water–cement rate was 0.35, the standard error of the mean was 0.46. This indicated that when the water–cement rate decreased, the tensile strength of the Stratabinder HS cement became scattered.

It is interesting to see that when conducting the STS test on the Stratabinder HS cement, the specimen showed different performance when two different water–cement rates were used. For the water–cement rate of 0.35, the bearing capacity of the specimen reached the final peak when the displacement was approximately 0.4 mm. Before that, an initial peak in the bearing capacity was reached. In contrast, when the water–cement rate was 0.42, only one peak in the bearing capacity occurred.

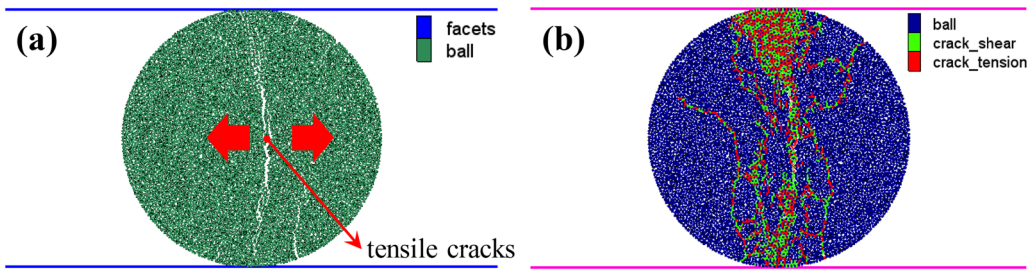

Fig. 19 Failure mode and crack state when the water–cement rate was 0.42: **a** failure mode; **b** crack state.

For this reason, the authors assumed that when the displacement reached approximately 0.2 mm, micro tensile cracks were generated along the vertical direction. This led to a sudden decrease in the bearing capacity. However, since the water–cement rate was 0.35, the pieces of the specimen had relatively high strengths. Therefore, these pieces could still join together to support the external loading force. Then, as the displacement increased, the bearing capacity of the specimen rose again.

Meanwhile, the micro tensile cracks continuously developed. Finally, when the displacement reached approximately 0.4 mm, these micro tensile cracks were connected. Consequently, macro tensile cracks were generated in the specimen. Moreover, the specimen was separated into two main parts. Before those two main parts separated thoroughly, the specimen bearing capacity reached the final peak. After that, the bearing capacity of the specimen was lost.

In contrast, for the water–cement rate of 0.42, when the displacement reached approximately 0.2 mm, micro tensile cracks were generated in the specimen along the vertical direction. This led to a decrease in the specimen bearing capacity. More importantly, since the water–cement rate was a high value of 0.42, the pieces of the specimen had a relatively low strength. Therefore, these pieces of the specimen were not able to join. Consequently, the specimen bearing capacity dropped continuously.

6 Conclusions

In this study, experimental and numerical mechanical tests were carried out on a modified Portland cement: Stratabinder HS cement. The stress–displacement, failure modes and stress state of the tested specimens were recorded and compared. The following conclusions were drawn:

(1) The water–cement rate significantly influenced the tensile performance of the cement paste. When the water–cement rate increased, the tensile strength of the cement paste apparently declined.
(2) During the STS test, the specimens consistently failed by generating vertical cracks at the middle section of the specimen. This failure mode was independent of the water–cement rate.
(3) The DEM method was effective in simulating the failure process of the cement paste. Based on calibration, the stress–displacement curve and failure mode of the specimen agreed well with the experimental test. According to the numerical simulation, during the STS test, not only tensile cracks but also shear cracks occurred in the specimen.
(4) In the STS test, before the tensile stress reached the peak, the number of fractures increased slightly. However, after the peak, the crack quantity increased dramatically. During the STS test, fractures mainly developed in the postpeak stage.
(5) During the vertical STS test, apparent horizontal tensile stress occurred in the specimen. Before the tensile stress reached the tensile strength, the horizontal tensile stress zone showed a diamond shape. The higher the tensile stress is, the larger the area of the diamond-shaped tensile stress zone. When the tensile stress reached the peak, the horizontal tensile stress was mainly concentrated in the vertical centre of the specimen. After tensile strength testing, apparent vertical cracks occurred. Then, particles in the cement paste lost the ability to bear the tensile stress.

7 Recommendations for Further Work

Further studies will continue to develop an effective method to conduct a direct UTS test on cement paste. Numerical simulation of the UTS test will also be conducted as a supplementary method to evaluate the failure behaviour and stress state of the cement paste.

Abbreviations

DEM: Discrete element method;; PFC: Particle flow code;; SD: Standard deviation;; SEM: Standard error of the mean;; STS: Split tensile strength;; UCS: Uniaxial compressive strength;; UTS: Uniaxial tensile strength.

Author Contributions

Conceptualisation: JZ and DL; writing: JC, KT, BZ, LL, and HZ. All authors read and approved the final manuscript.

Authors' Information

Jianhang Chen—Associate professor, State Key Laboratory for Geomechanics and Deep Underground Engineering, China University of Mining and Technology (Beijing), Beijing, 100083, China.
Kangming Tao—Graduate student, School of Energy and Mining Engineering, China University of Mining and Technology (Beijing), Beijing, 100083, China.
Banquan Zeng—Graduate student, School of Energy and Mining Engineering, China University of Mining and Technology (Beijing), Beijing, 100083, China.
Lei Liu—Graduate student, School of Energy and Mining Engineering, China University of Mining and Technology (Beijing), Beijing, 100083, China.
Hongbao Zhao—Professor, School of Energy and Mining Engineering, China University of Mining and Technology (Beijing), Beijing, 100083, China.
Junwen Zhang—Professor, School of Energy and Mining Engineering, China University of Mining and Technology (Beijing), Beijing, 100083, China.
Danqi Li—Lecturer, WA School of Mines: Minerals, Energy and Chemical Engineering, Curtin University, Kalgoorlie, WA, 6430, Australia.

Funding

National Natural Science Foundation of China (52034009, 51904302, 52174093), Opening funding by State Key Laboratory for Geomechanics and Deep Underground Engineering, CUMTB (SKLGDUEK2122), Yue Qi Distinguished Scholar Project (800015Z1179) and Fundamental Research Funds for the Central Universities (2022YQNY08).

Availability of Data and Materials
All data, models, and codes generated or used during the study appear in the submitted article.

Declarations

Competing Interests
No.

Author details
[1]State Key Laboratory for Geomechanics and Deep Underground Engineering, China University of Mining and Technology (Beijing), Beijing 100083, China. [2]School of Energy and Mining Engineering, China University of Mining and Technology (Beijing), Beijing 100083, China. [3]Energy and Chemical Engineering, WA School of Mines: Minerals, Curtin University, Kalgoorlie, WA 6430, Australia.

Received: 20 February 2022 Accepted: 4 July 2022
Published online: 14 November 2022

References

Aili, A., & Maruyama, I. (2020). Review of several experimental methods for characterization of micro- and nano-scale pores in cement-based material. *International Journal of Concrete Structures and Materials, 14*(1), 1–18. https://doi.org/10.1186/s40069-020-00431-y

Aziz, N., Majoor, D., & Mirzaghorbanali, A. (2017). Strength properties of grout for strata reinforcement. *Procedia Engineering, 191*(2017), 1178–1184. https://doi.org/10.1016/j.proeng.2017.05.293

Bayindir, F., Akyil, M., & Bayindir, Y. Z. (2009). Effect of storage pH on compressive and diametral tensile strength of adhesive luting cements. *Materials Research Innovations, 13*(2), 124–128. https://doi.org/10.1179/143307509X435673

Bitouri, Y. E., Jamin, F., & Youssoufi, M. S. E. (2017). Tensile and shear bond strength between cement paste and aggregate subjected to high temperature. *Materials and Structures, 50*(6), 1–9. https://doi.org/10.1617/s11527-017-1105-8

Bybee, K. (2004). Analysis of tensile-strength test methods for oilfield cement. *Journal of Petroleum Technology, 56*(8), 62–64. https://doi.org/10.2118/0804-0062-JPT

Chen, J., & Li, D. (2022). Numerical simulation of fully encapsulated rock bolts with a tri-linear constitutive relation. *Tunnelling and Underground Space Technology, 120*, 1–13. https://doi.org/10.1016/j.tust.2021.104265

Chen, X., Wu, S., & Zhou, J. (2013). Influence of porosity on compressive and tensile strength of cement mortar. *Construction and Building Materials, 40*, 869–874. https://doi.org/10.1016/j.conbuildmat.2012.11.072

Chen, Y., Zuo, J., Liu, D., & Wang, Z. (2019). Deformation failure characteristics of coal-rock combined body under uniaxial compression: Experimental and numerical investigations. *Bulletin of Engineering Geology and the Environment, 78*, 3449–3464. https://doi.org/10.1007/s10064-018-1336-0

Chen, Y., Teng, J., Bin Sadiq, R. A., & Zhang, K. (2020). Experimental study of bolt-anchoring mechanism for bedded rock mass. *International Journal of Geomechanics, 20*(4), 1–12. https://doi.org/10.1061/(ASCE)GM.1943-5622.0001561

Chen, J., Zhao, Y., Zhao, H., Zhang, J., Zhang, C., & Li, D. (2021). Analytic study on the force transfer of full encapsulating rockbolts subjected to tensile force. *International Journal of Applied Mechanics, 13*(9), 1–13. https://doi.org/10.1142/S1758825121500976

Chen, J., Liu, P., Liu, L., Zeng, B., Zhao, H., Zhang, C., Zhang, J., & Li, D. (2022). Anchorage performance of a modified cable anchor subjected to different joint opening conditions. *Construction and Building Materials, 336*, 1–12. https://doi.org/10.1016/j.conbuildmat.2022.127558

Fedrigo, W., Núñez, W. P., López, M. A. C., Kleinert, T. R., & Ceratti, J. A. P. (2018). A study on the resilient modulus of cement-treated mixtures of RAP and aggregates using indirect tensile, triaxial and flexural tests. *Construction and Building Materials, 171*, 161–169. https://doi.org/10.1016/j.conbuildmat.2018.03.119

Gu, C., Xu, J. Y., & Meng, B. X. (2019). Effect of saturation on mechanical behavior of cement mortar based on 8-type tensile test. *IOP Conference Series: Earth and Environmental Science, 267*, 1–7. https://doi.org/10.1088/1755-1315/267/2/022003

Jung, S., Saraswathy, V., Karthik, S., Kathirvel, P., & Kwon, S.-J. (2018). Microstructure characteristics of fly ash concrete with rice husk ash and lime stone powder. *International Journal of Concrete Structures and Materials, 12*(2), 279–287. https://doi.org/10.1186/s40069-018-0257-4

Li, D., Masoumi, H., & Ming, C. (2021). A constitutive model for modified cable bolts exhibiting cone shaped failure mode. *International Journal of Rock Mechanics and Mining Science, 145*, 104855. https://doi.org/10.1016/j.ijrmms.2021.104855

Liu, P., Zhou, X., Qian, Q., Berto, F., & Zhou, L. (2019). Dynamic splitting tensile properties of concrete and cement mortar. *Fatigue and Fracture of Engineering Materials and Structures, 43*(4), 757–770. https://doi.org/10.1111/ffe.13162

Masoud, G., Ali, B., & Mostafa, K. (2010). Residual mechanical properties of high-strength concretes after exposure to elevated temperatures. *Journal of Materials in Civil Engineering, 22*(1), 59–64. https://doi.org/10.1061/(ASCE)0899-1561(2010)22:1(59)

Mishra, P. K., & Kantharia, M. (2021). Tensile strength investigation of cement mortar using Nano zinc oxide (ZnO). *Materials Today: Proceedings, 47*, 7178–7180. https://doi.org/10.1016/j.matpr.2021.06.402

Murmu, M., & Singh, S. P. (2014). Hydration products, morphology and microstructure of activated slag cement. *International Journal of Concrete Structures and Materials, 8*(1), 61–68. https://doi.org/10.1007/s40069-013-0056-x

Němeček, J., Králíka, V., Šmilauera, V., Polívkab, L., & Jägerb, A. (2016). Tensile strength of hydrated cement paste phases assessed by micro-bending tests and nanoindentation. *Cement and Concrete Composites, 73*, 164–173. https://doi.org/10.1016/j.cemconcomp.2016.07.010

Paknahad, A., Kucko, N. W., Leeuwenburgh, S. C. G., & Sluys, L. J. (2020). Experimental and numerical analysis on bending and tensile failure behavior of calcium phosphate cements. *Journal of the Mechanical Behavior of Biomedical Materials, 103*, 1–16. https://doi.org/10.1016/j.jmbbm.2019.103565

Rashad, A. M., Seleem, H.E.-D.H., & Shaheen, A. F. (2014). Effect of Silica Fume and Slag on Compressive Strength and Abrasion Resistance of HVFA Concrete. *International Journal of Concrete Structures and Materials, 8*(1), 69–81. https://doi.org/10.1007/s40069-013-0051-2

Şahin, H. G., Biricik, Ö., & Mardani-Aghabaglou, A. (2022). Polycarboxylate-based water reducing admixture - clay compatibility; literature review. *Journal of Polymer Research, 29*(33), 1–19. https://doi.org/10.1007/s10965-021-02884-5

Silvestro, L., & Gleize, P. J. P. (2020). Effect of carbon nanotubes on compressive, flexural and tensile strengths of Portland cement-based materials: A systematic literature review. *Construction and Building Materials, 264*, 1–12. https://doi.org/10.1016/j.conbuildmat.2020.120237

Skrzypkowski, K. (2021). An experimental investigation into the stress-strain characteristic under static and quasi-static loading for partially embedded rock bolts. *Energies, 14*(5), 1–17. https://doi.org/10.3390/en14051483

Song, Z., & Zhang, J. (2022). Research on the progressive failure process and fracture mechanism of rocks with the structural evolution perspective. *Journal of Structural Geology, 154*, 1–12. https://doi.org/10.1016/j.jsg.2021.104484

Sun, W., & Wu, S. (2021). A study of crack initiation and source mechanism in the Brazilian test based on moment tensor. *Engineering Fracture Mechanics, 246*, 1–23. https://doi.org/10.1016/j.engfracmech.2021.107622

Syarif, M., Sampebulu, V., & Tjaronge, M. W. (2018). Characteristic of compressive and tensile strength using the organic cement compare with portland cement. *Case Studies in Construction Materials, 9*, 1–9. https://doi.org/10.1016/j.cscm.2018.e00172

Wang, S., Chen, F., Xue, Q., & Zhang, P. (2020). Splitting tensile strength of cement soil reinforced with basalt fibers. *Materials, 13*(14), 1–15. https://doi.org/10.3390/ma13143110

Wang, Z., Wang, T., Wu, S., & Hao, Y. (2021). Investigation of microcracking behaviors in brittle rock using polygonal grain-based distinct method. *International Journal for Numerical and Analytical Methods in Geomechanics, 45*(13), 1871–1899. https://doi.org/10.1002/nag.3246

Wu, S., Chen, H., Ramandi, F. L., Hagan, P. C., Hebblewhite, B., Crosky, A., & Saydam, S. (2018). Investigation of cable bolts for stress corrosion cracking failure. *Construction and Building Materials, 187*, 1224–1231. https://doi.org/10.1016/j.conbuildmat.2018.08.066

Wu, S., Ramandi, H. L., Chen, H., Crosky, A., Hagan, P. C., & Saydam, S. (2019). Mineralogically influenced stress corrosion cracking of rockbolts and cable bolts in underground mines. *International Journal of Rock Mechanics and Mining Sciences, 119*, 109–116. https://doi.org/10.1016/j.ijrmms.2019.04.011

Xiong, L., & Geng, D. (2020). Scale effect of cement mortar specimens subjected to high temperatures using uniaxial compressive and splitting tensile tests. *Archives of Civil Engineering, LXVI*(3), 139–155. https://doi.org/10.24425/ace.2020.134389

Chen, J., Hagan, P. C., & Saydam, S. (2014). Mechanical properties of cementitious grout serving in fully grouted cable bolting systems. AusRock 2014: Third Australasian ground control in mining conference, Sydney, Australia, pp. 269–275.

Hyett, A. J., Bawden, W. F., & Coulson, A. L. (1992). Physical and mechanical properties of normal Portland cement pertaining to fully grouted cable bolts. In: Proceedings of the International symposium on rock support, Sudbury, Canada, pp. 341–348.

Rocha, V. V., & Ludvig, P. (2017). Characterization of Portland cement composites prepared by a dispersion of carbon nanotubes on cement particles. In: 12th central european congress on concrete engineering, Tokaj, Hungary, pp. 195–201.

Publisher's Note